Astronomy & Astrophysics

Type II radio bursts and their association with coronal mass ejections in solar cycles 23 and 24

A. Kumari[1,2] , D. E. Morosan[1], E. K. J. Kilpua[1], and F. Daei[1]

[1] Department of Physics, University of Helsinki, PO Box 64, 00014 Helsinki, Finland
e-mail: anshu.kumari@helsinki.fi
[2] NASA Postdoctoral Program Fellow, NASA Goddard Space Flight Center, Greenbelt, MD 20771, USA

ABSTRACT

Context. Meter-wavelength type II solar radio bursts are thought to be the signatures of shock-accelerated electrons in the corona. Studying these bursts can give information about the initial kinematics, dynamics, and energetics of coronal mass ejections (CMEs) in the absence of white-light observations.
Aims. We investigate the occurrence of type II bursts in solar cycles 23 and 24 and their association with CMEs. We also explore whether type II bursts might occur in the absence of a CME.
Methods. We performed a statistical analysis of type II bursts that occurred between 200 and 25 MHz in solar cycles 23 and 24 and determined the temporal association of these radio bursts with CMEs. We categorized the CMEs based on their linear speed and angular width and studied the distribution of type II bursts with fast ($\geq$500 km s^{-1}), slow ($<$500 km s^{-1}), wide ($\geq$60°), and narrow ($<$60°) CMEs. We explored the dependence of type II bursts occurrence on the phases of the solar cycle.
Results. Our analysis shows that during solar cycles 23 and 24, 768 and 435 type II bursts occurred, respectively. Of these, 79% were associated with CMEs in solar cycle 23, and 95% were associated with CMEs in solar cycle 24. However, only 4% and 3% of the total number of CMEs were accompanied by type II bursts in solar cycle 23 and 24, respectively. Most of the type II bursts in both cycles were related to fast and wide CMEs (48%). We also determined the typical drift rate and duration for type II bursts, which is 0.06 MHz s^{-1} and 9 min. Our results suggest that type II bursts dominate at heights $\approx$1.7–2.3 $\pm$ 0.3 $R_\odot$. A clear majority have an onset height around 1.7 $\pm$ 0.3 $R_\odot$ assuming the four-fold Newkirk model.
Conclusions. The results indicate that most of the type II bursts had a white-light CME counterpart, but a few type II bursts lacked a clear CME association. There were more CMEs in cycle 24 than in cycle 23. However, cycle 24 contained fewer type II radio bursts than cycle 23. The onset heights of type II bursts and their association with wide CMEs reported in this study indicate that the early lateral expansion of CMEs may play a key role in the generation of these radio bursts.

Key words. Sun: activity – Sun: corona – Sun: coronal mass ejections (CMEs) – Sun: radio radiation – sunspots

1. Introduction

Coronal mass ejections (CMEs) can be powerful drivers of plasma shocks that can accelerate electrons to high energies. Accelerated electron beams in turn can generate radio bursts at meter and decimeter wavelengths through the plasma emission mechanism. Radio-shock signatures associated with CMEs are categorized as type II radio bursts (Smerd 1970; Dulk 1970; Klassen et al. 2002; Gopalswamy et al. 2005; Ramesh et al. 2023). Type II radio bursts are characterized as lanes of emission drifting from high to low frequencies in the solar dynamic spectra, with a duration of a few minutes to approximately one hour. These lanes have a frequency ratio of 1–2, representing emission at the fundamental and harmonic of the plasma frequencies (Nelson & Melrose 1985). Radio imaging and spectroscopy combined with coronal modeling have shown that type II bursts are associated with CME-driven shock waves (e.g., Smerd 1970; Ramesh et al. 2010; Zucca et al. 2018; Kumari et al. 2019). Type II bursts can also consist of numerous fine structures. For example, herringbone bursts are narrow bursts in dynamic spectra that are superimposed on type II bursts or that occur on their own, drifting toward higher and lower frequencies (Roberts 1959; Cairns & Robinson 1987;

Carley et al. 2015). Herringbone bursts are thought to be the radio signature of individual electron beams that are accelerated by the CME shock (Zlobec et al. 1993; Morosan et al. 2019). A wide variety of other fine structures composing the emission lanes of type II bursts have recently been documented in Magdalenić et al. (2020).

Type II bursts are the most common radio bursts accompanying CMEs. These bursts are therefore often used to study the kinematics, energetics, and dynamics of CMEs near the Sun (Cunha-Silva et al. 2015; Kumari et al. 2017c; Ma & Chen 2020). The advancement of space-based coronagraphs and ground-based spectrographs in the past two decades helped us to understand the relation between CMEs and meter-wavelength type II radio bursts. Metric type II bursts typically start at $\approx$1.5 $R_\odot$ (Lin et al. 2006). Claßen & Aurass (2002) studied the association of metric and interplanetary (IP) type II bursts with CMEs observed with LASCO for 63 events during 1997–2000, where the authors related the type II origin to blast-wave shocks or the leading edge or flanks of the CMEs. Gopalswamy (2006) performed a similar study for metric and decameter-hectometer (DH) type II bursts during 1996–2004. The author concluded that the metric type II bursts are mostly associated with slow CMEs and DH type II are associated with CMEs
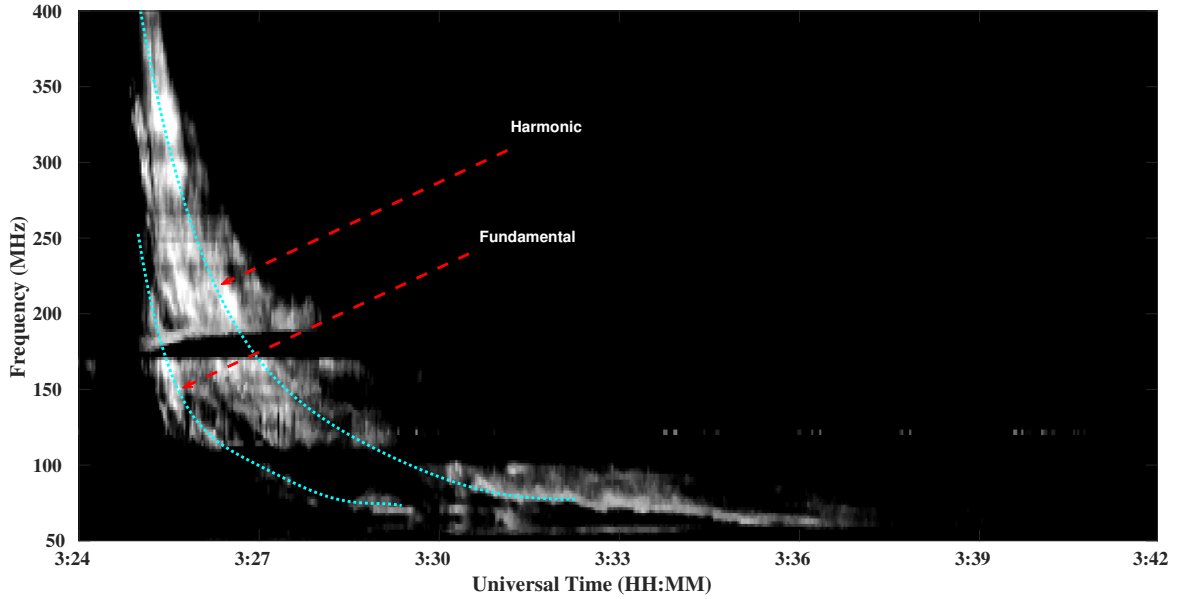
Fig. 1. Solar radio dynamic spectra of a high-frequency type II burst on November 4, 2015. The duration of the burst is ≈12 min, and it shows a frequency drift of ≈0.2 MHz s^{-1} from 400 MHz to 55 MHz. The cyan lines show the fundamental and harmonic bands in the spectra.

with speed >1100 km s^{-1}. Kahler et al. (2019) also studied metric and DH type II bursts and their association with solar energetic particles (SEPs) and found that it is uncommon for these events to be associated with fast and narrow CMEs. Recently, Pohjolainen & Talebpour Sheshvan (2021) studied isolated DH type II radio bursts, which were found to be associated with a shock near the CME leading front.

However, at present, there is no comprehensive long-term statistical study of metric type II bursts and their relation with CMEs that covers over one solar cycle. Recently, Morosan et al. (2021) studied moving radio bursts, which include type II and moving type IV bursts, and their association with CMEs, and found that moving radio sources are almost exclusively associated with CME eruptions. Patel et al. (2021) studied decameter-hectometer type II bursts and concluded that the initial speed of a CME is related to the duration of type II bursts. With the end of solar cycle 24 and the availability of white-light CME and type II radio bursts data for more than two decades, we take this opportunity to study the association of type II bursts with CMEs for the last two solar cycles, cycles 23 and 24, and determine the general properties of these CMEs and the associated radio emission. This article is arranged as follows: Sect. 2 reports the details of the observational data and the data analysis methods. We discuss the results we obtained with our analysis in Sect. 3. We present the summary and conclude in Sect. 4.

2. Observations and data analysis

We used the CMEs listed in the Coordinated Data Analysis Workshop (CDAW; Yashiro et al. 2004, 2008; Gopalswamy et al. 2009b) database[1], which lists the CMEs that were manually detected with the Large Angle and Spectrometric Coronagraph (LASCO) on board the Solar and Heliospheric Observatory (SOHO; Brueckner et al. 1995). This list contains the CMEs detected with the LASCO coronagraphs since January 1996. It includes CME properties such as the linear and second-order speed, position angle, acceleration, mass, and

kinetic energy. We also used the Cor1 and Cor2 coronagraphs from the Sun-Earth Connection Coronal and Heliospheric Investigation (SECCHI; Howard et al. 2008) on board the Solar Terrestrial Relationship Observatory (STEREO). For the CMEs observed with the STEREO spacecrafts, we used the list provided on the Solar Eruptive Event Detection System (SEEDS)[2] website. The CMEs listed here are detected automatically using software packages that extract the position angle, angular width, velocity, peak, and average brightness (Olmedo et al. 2008). We also used the CME list provided by Vourlidas et al. (2017), where the authors used the dual-viewpoint CME catalog from the SECCHI/COR telescopes[3]. These catalogs contain STEREO-detected CMEs from 2009 to 2014.

For the radio data, we used the event lists provided by the Space Weather Prediction Center (SWPC)[4]. These event lists contain details of the solar eruptions, such as X-ray and optical flares, radio burst types and their proprieties, the start and end time of the eruption, the class of the flares, and the frequency of the radio bursts. We also used sunspot data to investigate the correlation between the appearance of sunspots and the occurrence of type II bursts. The sunspot data were taken from the SILSO World Data Center (1996–2019)[5], which has daily, monthly mean, and 13-month-averaged sunspot data available.

In this work, we investigate the relation between type II bursts and CMEs in solar cycles 23 and 24. To do this, we extracted the type II burst information from the SWPC event lists from January 1996 to December 2019. This exclusive type II burst list contains all the type II bursts in solar cycles 23 and 24, with details such as the start and end time, the start and end frequency, the reporting spectrograph, and the associated active region (AR). An example of a type II burst is shown in Fig. 1a. This figure shows a high-frequency high-drift

---

Table 1. Year-wise distribution of CMEs, type II radio bursts, and their association.

Year	CMEs	% CMEs	Type IIs	% Type IIs	Type IIs with CMEs	% Type IIs with CMEs	Type IIs without CME	% Type IIs without CME
Total	30 125	100.0%	1203	100.0%	1024	85.2%	179	14.8%
1996	206	1.5%	4	0.5%	2	0.3%	2	1.2%
1997	385	2.7%	21	2.7%	16	2.6%	5	3.1%
1998	716	5.1%	60	7.8%	24	3.9%	36	22.6%
1999	1016	7.2%	100	13.0%	75	12.3%	25	15.7%
2000	1664	11.9%	90	11.7%	72	11.8%	18	11.3%
2001	1499	10.7%	160	20.8%	136	22.3%	24	15.1%
2002	1700	12.1%	116	15.1%	96	15.8%	20	12.6%
2003	1130	8.1%	71	9.2%	62	10.2%	9	5.7%
2004	1102	7.9%	69	9.0%	58	9.5%	11	6.9%
2005	1248	8.9%	49	6.4%	45	7.4%	4	2.5%
2006	1047	7.5%	19	2.5%	15	2.5%	4	2.5%
2007	1442	10.3%	7	0.9%	6	1.0%	1	0.6%
2008	863	6.1%	2	0.3%	2	0.3%	0	0.0%
Total (cycle 23)	14 018	100.0%	768	100.0%	609	79.3%	159	20.7%
2009	746	4.6%	1	0.2%	1	0.0%	0	0.0%
2010	1117	6.9%	13	3.0%	13	3.1%	0	0.0%
2011	1990	12.4%	72	16.5%	68	16.4%	4	20.0%
2012	2177	13.5%	71	16.3%	69	16.6%	2	10.0%
2013	2338	14.5%	73	16.9%	72	17.3%	1	5.0%
2014	2478	15.4%	110	25.3%	102	24.6%	8	40.0%
2015	2058	12.8%	54	12.4%	51	12.9%	3	15.0%
2016	1393	8.7%	15	3.4%	15	3.6%	0	0.0%
2017	786	4.9	18	4.1%	6	4.1%	1	5.0%
2018	476	2.9%	2	0.5%	2	0.5%	0	0.0%
2019	543	3.4%	6	1.4%	1	1.2%	1	5.0%
Total (cycle 24)	16 107	100.0%	435	100.0%	415	95.4%	20	4.6%

type II burst that occurred on November 4, 2015. The solar dynamic spectra shown here were taken with the ground-based Compound Astronomical Low-cost Low-frequency Instrument for Spectroscopy and Transportable Observatory (CALLISTO)[6] spectrometer at the Gauribidanur Radio Observatory (GRO)[7]. The fundamental and harmonic bands are the type II bursts, and they are marked in the figure.

To determine the associations of type II bursts with CMEs, we used the criteria that the start time of the associated CME should be within 2 h of the start time of the type II burst. This time difference between the start times of type IIs and CMEs was chosen in order to compensate for disk events, where the CME may be seen later in white-light images compared to limb events (e.g., Kumari et al. 2021; Morosan et al. 2021; Kumari 2022). Two new lists were prepared based on these criteria, which contain the information of (i) type II bursts associated with CMEs and (ii) type II bursts without any association with CMEs. These two lists were used to further carry out our study.

3. Results

The yearly distribution of CMEs and type II radio bursts and the percentage of type II bursts with and without CMEs are shown in Table 1. During solar cycles 23 and 23, 768 and 435 type II bursts were reported, respectively. During solar cycles 23 and 24, 14 018 and 16 107 CMEs were reported during respectively (based on LASCO white-light observations). An additional 5944

---

6 http://www.e-callisto.org/
7 https://www.iiap.res.in/centers/radio

CMEs were recorded with the STEREO coronagrapghs (A and B combined) in solar cycle 24.

The results in Table 1 are also illustrated in Fig. 2, which shows the histograms of the occurrence of CMEs and type II bursts in cycles 23 and 24. We fit a Gaussian to these distributions, which showed that the CMEs and type II events both peak during solar cycle maxima, that is, during 2000–2002 and 2013–2014 for cycle 23 and 24, respectively. We note that more CMEs occurred during the declining than during the rising phase of cycle 23. Almost ≈24% of the CMEs in cycle 23 were recorded during the decline phase. In contrast, more CMEs occurred during the rising phase of cycle 24 than during the declining phase. However, both cycles showed a similar trend for type II radio bursts, where there were more bursts at the beginning of the cycle than at the end of the cycle. This indicates that the occurrence of the type II bursts follows the same pattern as the sunspot cycle.

3.1. Type II bursts and associated CMEs

In cycle 23, ≈79% type II bursts were associated with a white-light CME using our criteria, while in cycle 24, the percentage was considerably higher, ≈95%s. However, the fraction of CMEs associated with type II bursts was more similar and very low, only ≈4% and ≈3% in solar cycles 23 and 24, respectively. The lower association of type II bursts with CMEs in solar cycle 23 could be explained by two possibilities: (i) the unavailability of the STEREO spacecraft, which were available during solar cycle 24 to provide different view points, making it possible to identify more CMEs, especially those originating from the far side of the Sun; and (ii) the loss of contact of LASCO during 1998, when
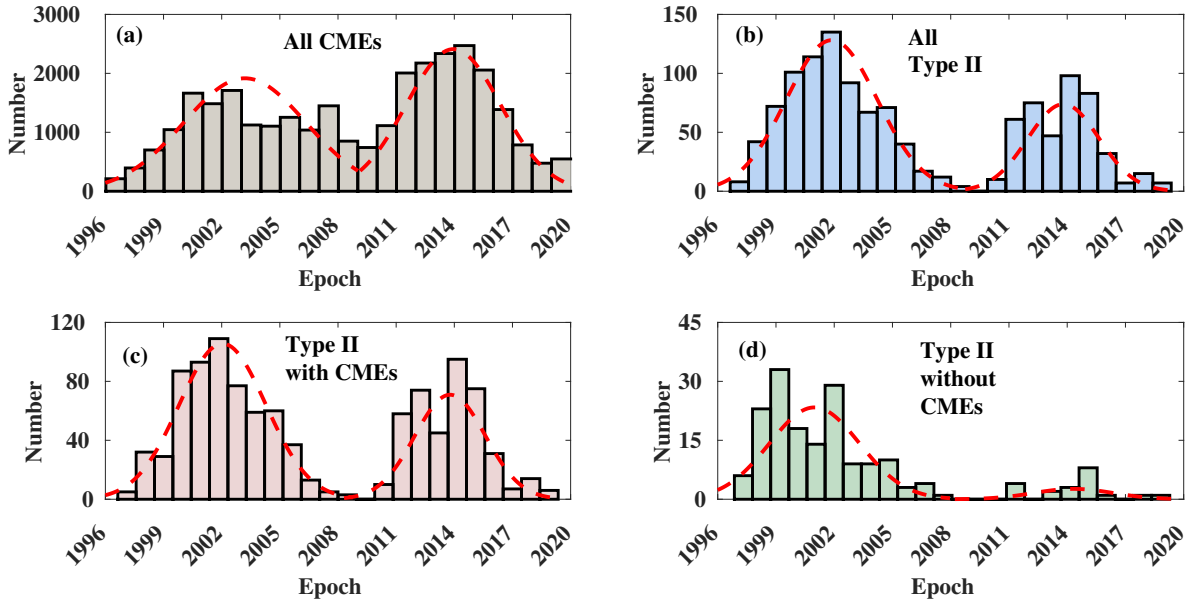
Fig. 2. Histograms showing the distribution of the occurrence of (a) all CMEs, (b) all type II bursts, (c) all type II bursts that were accompanied with white-light CMEs, and (d) all type II bursts without any association with a CME from January 1996, to December 2019. This corresponds to solar cycles 23 and 24. The dashed red profile shows the Gaussian fit to the histograms. The two peaks of these Gaussian peaks correspond to the solar maxima in the respective solar cycles.

no white-light CME identifications could be made. We note that because of the loss of contact with STEREO-B during SC4, we could not use it for the type II and CME association. Figure 2 (bottom panel) shows the distribution of the occurrence of type II bursts with and without any CME association. The Gaussian fits show a similar pattern, in which the peaks coincide with the peak of the solar cycle. Table 1 also shows the type II–CME association for both cycles.

3.2. Type II bursts associated with the CME type

We categorized the CMEs on the basis of their linear speeds and angular width as fast, slow, wide, and Narrow CMEs (Kumari et al. 2021; Morosan et al. 2021). The CMEs with linear speed $\geq$500 km s^{-1} were classified as fast CMEs, and the rest were kept in the slow CME category. Similarly, CMEs with an angular width $\geq$60° were designated wide CMEs and the rest were narrow CMEs. Table 2 contains the list of type II bursts associated with different types of CMEs.

We found that most of the type II bursts were associated with fast and wide CMEs, regardless of the cycle ($\approx$48%). Figure 3 shows histograms of the distribution of type II bursts associated with various CME types. The Gaussian distributions to the dataset peak during solar maximum for fast, slow, wide, and narrow CMEs for both solar cycles. We note that fast and slow CMEs were distributed almost equally in the past two cycles, but most of the type II bursts were associated with wide CMEs. The bottom panel of Fig. 3 also shows the type II bursts for a combination of speed and width of CMEs. Only very few type II bursts were associated with fast and narrow CMEs. Figure 3 and Table 2 show that the type II burst association with CMEs follows the same pattern in both solar cycles.

We note that we considered the linear speed of CMEs as mentioned in the CME catalogs used in this study. A constant linear speed has projection effects, and it does not include the complete kinematics of CMEs in the solar atmosphere. However, we used an average linear speed for CMEs because more than

30 000 CMEs are included in our study. We acknowledge that this could lead to a few misclassification of the type of CMEs in this study. Several previous studies have reported that type II bursts are often related to the flanks of CMEs (Holman & Pesses 1983; Gopalswamy et al. 2009a; Kumari et al. 2017c). The CME speeds at the leading edge and flanks may vary, and individual case studies need to be carried out to verify the CME shock speed and type II association.

3.3. Type II bursts associated with halo and partial aalo CMEs

We studied the association of type II radio bursts with halo CMEs. Partial halo and halo CMEs are included in the wide CME category. CMEs with a width $W = 360°$ are classified as full halos, and those with a width $120° \leq W < 360°$ are classified as partial halos. Table 3 lists the type II bursts associated with partial and full halo CMEs in cycles 23 and 24. We found that more type II bursts were associated with partial and full halo CMEs in cycle 24 (26%) than in cycle 23, regardless of the fact that there were fewer type II bursts in the latter cycle. The halo CMEs were distributed almost equally as partial and full halos for both cycles. Figure 4 shows the distribution of type II bursts associated with partial halo, full halo, and other CMEs. The Gaussian fits to the distribution also follow a similar pattern as the previous distribution, that is, the peaks occur during the maxima of the respective solar cycles.

3.4. Type II bursts and their properties

We analyzed the spectral (time-frequency) properties of the type II bursts for solar cycles 23 and 24 using the type II burst list generated in Sect. 2. We estimated the duration of the type II bursts using the start and end time (t_{start} and t_{end}, respectively) as noted in the SWPC event lists. We also estimated the drift rates of these bursts using the start and end frequencies (f_{start} and f_{start}, respectively) as recorded in the solar dynamic spectra.

Table 2. Number and percentage of type II radio bursts associated with CMEs with different properties: Fast, slow, wide, narrow, and a combination of these properties.

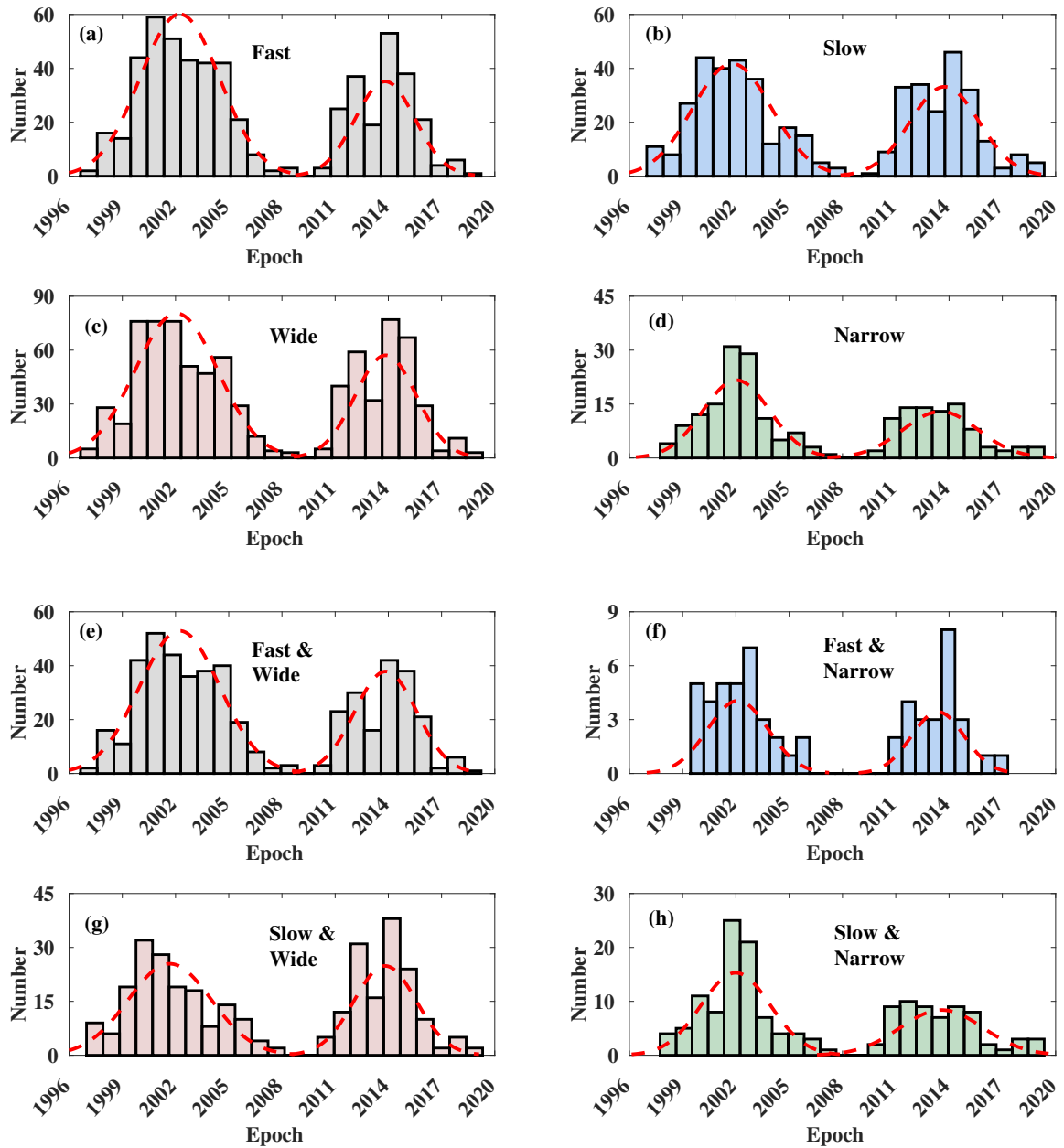| Category	Total		Cycle 23		Cycle 24	
	No.	%	No.	%	No.	%
Total	1024	100.0%	609	59.5%	415	40.5%
Fast	554	54.1%	347	57.0%	207	49.9%
Slow	470	45.9%	262	43.0%	208	50.1%
Wide	809	79.0%	482	79.1%	327	78.8%
Narrow	215	21.0%	127	20.9%	88	21.2%
Fast and wide	495	48.3%	313	51.4%	182	43.9%
Fast and narrow	59	5.8%	34	5.6%	25	6.0%
Slow and wide	314	30.7%	169	27.7%	145	34.9%
Slow and narrow	156	15.2%	93	15.3%	63	15.2%

Fig. 3. Histograms showing the variation in occurrence of type II bursts with (a) fast, (b) slow, (c) wide, (d) narrow, (e) fast and wide, (f) fast and narrow, (g) slow and wide, and (h) slow and narrow CMEs for solar cycles 23 and 24.

Table 3. Number and percentage of type II radio bursts associated with partial halo and halo CMEs.

Category	Total		Cycle 23		Cycle 24	
	No.	%	No.	%	No.	%
Total	1024	100.0%	609	59.5%	415	40.5%
Partial halo CMEs	241	23.5%	131	21.5%	110	26.5%
Halo CMEs	252	24.6%	144	23.6%	108	26.0%
Partial halo & Halo CMEs	493	48.1%	275	45.1%	218	52.5%
Other CMEs	531	51.9%	334	54.9%	197	47.5%
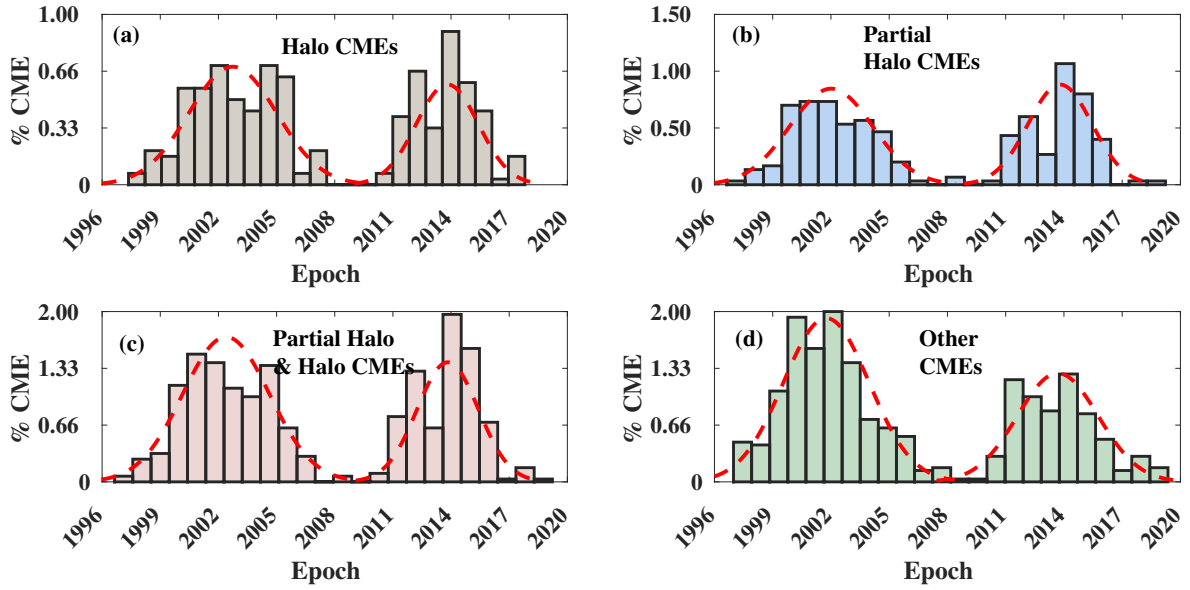
Fig. 4. Histograms showing the distribution of the occurrence type II bursts with (a) all halo CMEs, (b) all partial halo CMEs, (c) all partial halo and halo CMEs, and (d) all other CMEs from January 1996 to December 2019. This corresponds to solar cycles 23 and 24. The dashed red profile shows the Gaussian fit to the histograms. The two peaks of these Gaussian peaks correspond to the solar maxima in the respective solar cycles.

Figure 5 shows the distribution of the drift rate and duration of the type II bursts in the last two cycles. The drift rates of more than 90% of the type II bursts were higher than 0.05 MHz s^{-1} in both cycles for the frequency range 200–25 MHz. The behavior of these type II bursts is very similar to moving type IV bursts as reported by Kumari et al. (2021). Similarly, almost 80% of the bursts lasted shorter than 20 min. We note that type II bursts are slowing drifting features on the solar dynamic spectra. They can have different drift rates and in turn, different speeds in the solar atmosphere. We considered a constant drift rate for type II bursts, which can underestimate or overestimate the shock speed calculated from the radio burst.

3.5. Heights of type II bursts

We converted the start and end frequencies obtained for the type II busts from the SWPC events into heliocentric distances. We used the four-fold Newkirk density model to convert the frequency into heliocentric distance (Newkirk 1961; Mann et al. 1995). We used this model and the enhancement factor to account for the enhanced densities above active regions. There is always an ambiguity in using a particular density model because different density models and enhancement factors can reflect a range of possible heights of the radio sources. We began with the assumption that all the type II bursts were a fundamental-harmonic pair. The start frequency of the burst was therefore divided by a factor of two for a more accurate height estimation. The end frequency of the bursts was kept as it is because the end frequency of type II bursts is the end frequency of the fundamental lane. The speeds of the type II bursts were estimated using the height estimate and the duration (see Sect. 3.4) of the bursts. Figure 6 shows the histogram of the start and end frequencies of all the type II bursts we studied. For the type II bursts that were a fundamental-harmonic pair, we divided the start frequencies by a factor of two.

We first compared the speeds of the type II bursts to that of the associated CME. Figure 7a shows the linear correlation between the shock speed from radio bursts and the CME speed from white-light coronagraph data. There is almost no correlation (cc = 0.03) between the type II speed and the linear speed of the CME. The most likely cause for this lack of correlation is that the speed of the metric type II bursts reflects the speed at lower coronal heights ($\leq 2.5\,R_\odot$) compared to the CME linear speed mentioned in the CDAW catalog, which is obtained at much higher heights ($\geq 2.5\,R_\odot$). The type II speeds are also likely to be indicative of the lateral or flank speeds of CMEs and not of the radial outward speed because many metric type IIs have been reported to occur at the CME flank (Chrysaphi et al. 2018; Morosan et al. 2019; Majumdar et al. 2021). Another likely cause of the low correlation might be the
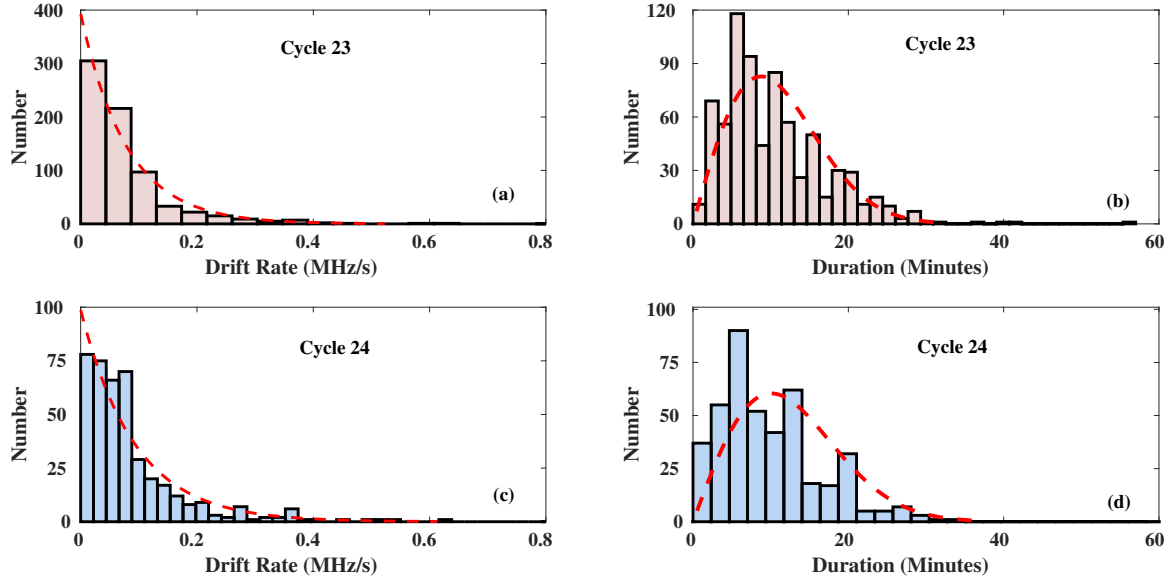
Fig. 5. Histograms showing the variation drift rates and duration of type II bursts in solar cycles 23 ((a) and (b), respectively) and 24 ((c) and (d), respectively).
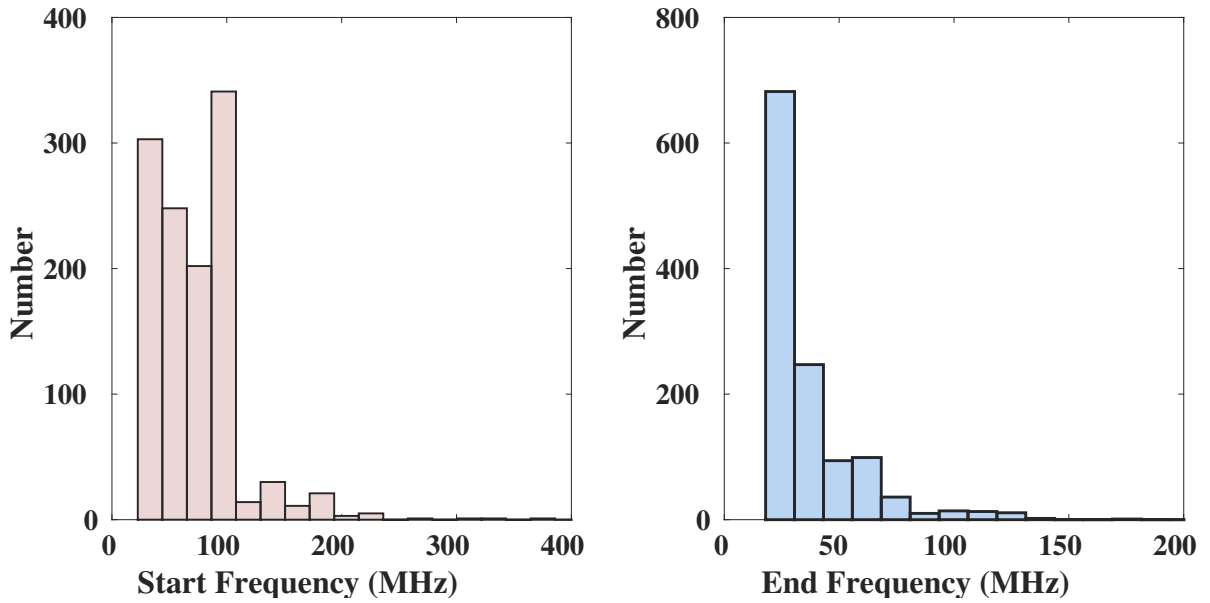

Fig. 6. Histograms showing the variation in the start (left panel) and end (right panel) frequencies of type II bursts in cycles 23 and 24. We have used the fundamental start frequency of all the type II bursts, as mentioned in Sect. 3.5. For the type II bursts that were a fundamental-harmonic pair, we divided the start frequencies by a factor of two.

assumption of a constant plane-of-sky CME speed. Figure 7b shows the distribution of type II heights over the years. We found that by using the four-fold Newkirk density model, the starting height of a large majority of type II bursts is at $\approx 1.7 \pm 0.3\,R_\odot$, as shown by the significant peak in Fig. 7b (for the frequency range $200-25$ MHz). The error bar indicates the variation in the type II height estimate while considering other density models, such as the Baumbach (Baumbach 1937, two-four fold) and Saito (Saito et al. 1977, two-six fold) models. This error bar is also similar to the standard deviation in the type II height estimates using the four-fold Newkirk model. Only a few metric type II bursts started at heights higher than $\approx 2.3\,R_\odot$ ($\leq 5\%$), which corresponds to frequencies below 50 MHz. Similarly, fewer type II bursts startied at low corona heights below $1.7\,R_\odot$. The majority

of type IIs have an onset height between 1.7 and $2.3\,R_\odot$, which indicates the height of plasma oscillations due to the electrons that are accelerated at the magnetohydrodynamics shocks in the solar corona.

3.6. Type II bursts, CMEs, and the correlation with sunspot number

Finally, we studied the relation between CMEs, type II bursts, and sunspot number (SSN) during the past two solar cycles. Figure 8a shows the correlation between the number of CMEs and type II bursts recorded per year. The correlation coefficient is low for cycle 23 (≈ 0.61), but type II bursts are highly correlated with CMEs for solar cycle 24 (the coefficient is ≈ 0.95).
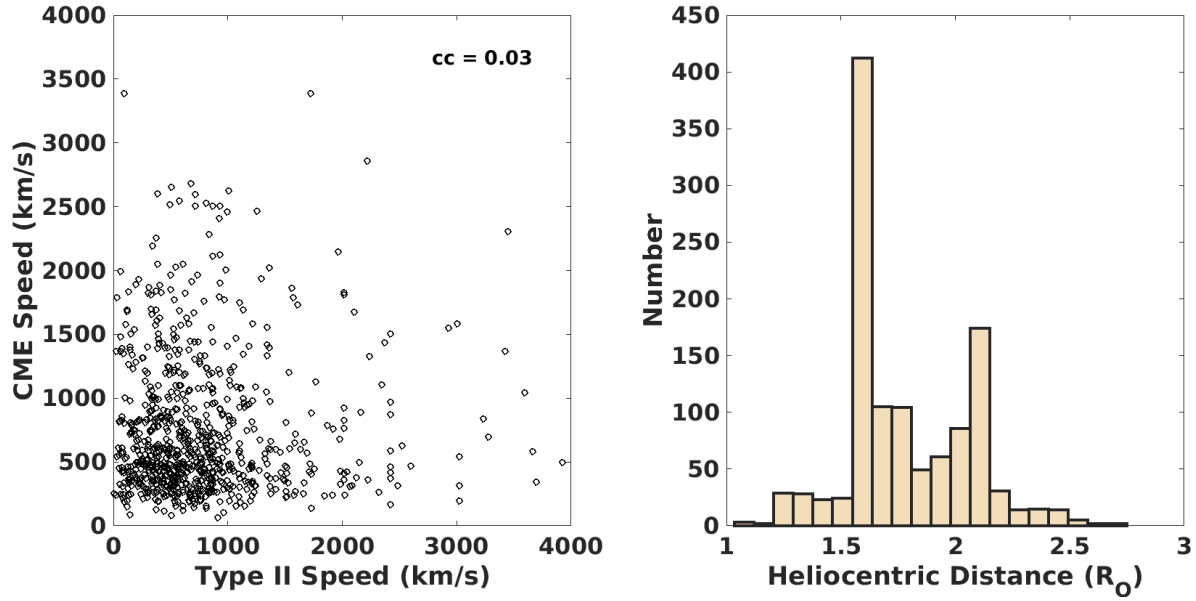
Fig. 7. Relation between CME linear speeds as mentioned in the catalog and the type II speed estimated with the four-fold Newkirk density model and the duration of the bursts (left panel) and distribution of the type II formation heights using the Newkirk density model (right panel).
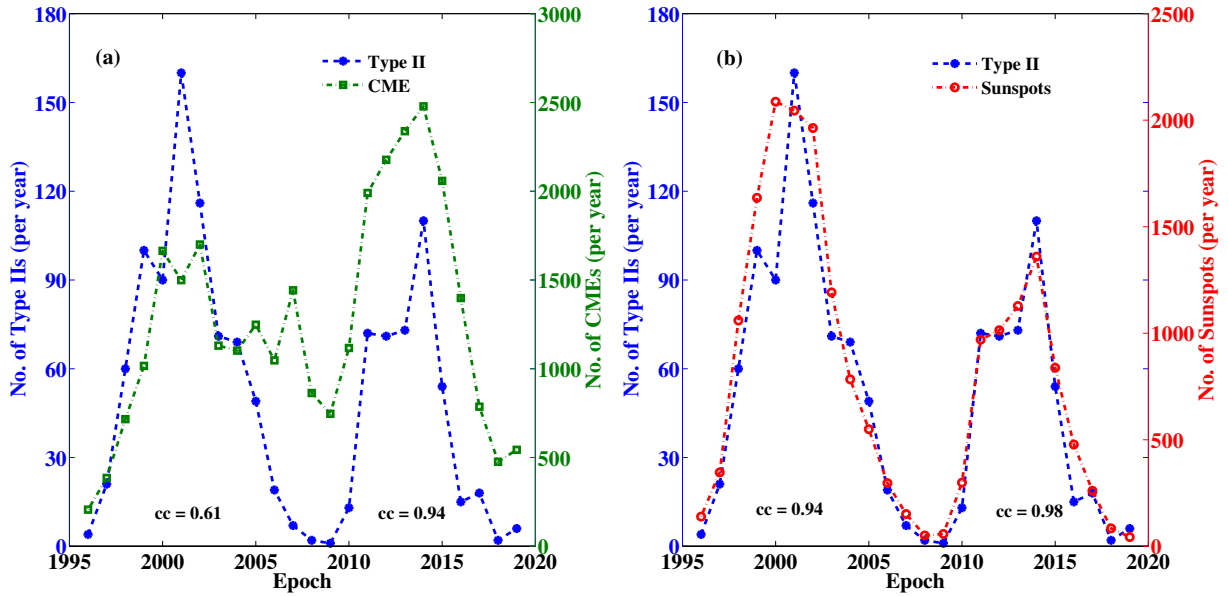

Fig. 8. Number of CMEs (per year) and type II bursts (per year) from 1996 to 2019 in the left panel and number of type II (per year) and sunspots (per year) in the right panel.

The sunspot numbers and type II bursts are also highly correlated in both cycles (≈0.94 and ≈0.98, respectively). Figure 8 also shows that these three phenomena are quite well correlated for cycle 24. Michalek et al. (2019) also showed that sunspot number and CMEs were poorly correlated for cycle 23 when compared to cycle 24. The correlation was improved when they removed poor CME events from their list.

4. Discussion

We presented the first comprehensive long-term analysis of the occurrence of metric type II radio bursts (low coronal radio bursts) during two solar cycles and their association with CMEs of various properties. We found that $\approx79\%$ and $\approx95\%$ of the type II bursts were associated with CMEs in solar cycles 23 and 24, respectively. However, only $\approx4\%$ and $\approx3\%$ of CMEs were associated with type II bursts in solar cycles 23 and 24, respectively. The results indicate that most of the type II bursts had a white-light CME counterpart, but a few type II bursts lacked a clear CME association. Some studies suggested that these type IIs may be related to flare-driven blast waves (Magdalenić et al. 2012; Kumar et al. 2016; Morosan et al. 2023). There were more CMEs in cycle 24 than in cycle 23. However, cycle 24 contained fewer type II radio bursts than cycle 23, thus a greater number of CMEs does not indicate that a greater number of type IIs would occur in a solar cycle. The type II occurrence also depends upon the CME properties, such as lateral expansion and speed, and on coronal conditions, such as the ambient magnetic fields (B), the Alfvén-Mach number (M_A), and the Alfvén speed (V_A) (Mann et al. 2003; Lin et al. 2006).

Almost 48% of the type II bursts were associated with fast and wide CMEs. This trend is similar to the type IV burst association with CMEs in cycle 24 (Kumari et al. 2021), and it was also found in the case of moving radio bursts (mostly type II and type IV bursts) in the study of Morosan et al. (2021). Only very few type II bursts were associated with slow and narrow CMEs. Morosan et al. (2021) suggested that fewer radio bursts associated with slow and narrow CMEs are observed because the generation of moving bursts (mostly consisting of type II and type IV bursts) is related to the lateral expansion during the early acceleration phase of a solar eruption.

Our analysis shows that almost half of the type II bursts in both solar cycles were accompanied by partial and full halo CMEs. They were essentially accompanied by very wide CMEs. Since it is well known that these CMEs might cause geomagnetic storms (Zhang et al. 2003), these type II bursts can be used to study the early kinematics of geoeffective halo CMEs. These radio bursts might also be useful in the case of stealth CMEs, whose early signatures are not visible in coronagraph images. So far, no account of a type II burst associated with a stealth CME has been reported, however. The correlation between type II bursts and sunspots is also high, indicating that type II bursts are associated with CMEs resulting from eruptive flares from sunspots and are less likely to be associated with phenomena such as filament eruptions, which do not require the presence of sunspots (Feynman & Hundhausen 1994; Choudhary & Moore 2003).

In comparison with other statistical studies of radio bursts, fewer type II bursts (435) were reported in cycle 24 than type IV bursts (447; Kumari et al. 2021). The reason might be that for type IV emission, shock is not an essential requirement, unlike for type II events (Salas-Matamoros & Klein 2020). In turn, more type II bursts were associated with CMEs than type IV bursts. However, based on this and previous studies (for example, see Kahler et al. 2019; Kumari et al. 2021; Morosan et al. 2021), it can be stated that both type II and type IV bursts are mostly associated with fast and wide CMEs.

Our results suggest that type II bursts dominate at a height of $\approx 1.7-2.3 \pm 0.3\,R_\odot$ (between 200 and 25 MHz), with a clear majority having an onset height around $1.7 \pm 0.3\,R_\odot$ assuming the four-fold Newkirk model. This height range indicates that there may be a critical height for a type II occurrence for the majority of solar eruptions. Similar results were found in a theoretical study by Lin et al. (2006), who suggested that type II bursts typically occur at a height of $1.5\,R_\odot$, which is similar to the heights reported in the present work for the majority of type II bursts. The authors modeled a CME with a terminal speed of approximately $1000\,\mathrm{km\,s^{-1}}$, using the magnetic field strength and a constant magnetic reconnection rate to obtain this height. Lin et al. (2006) suggested that type II bursts cannot appear lower than a critical height, which depends upon then coronal environment and determines the start frequency of the burst. The critical height is likely highly dependent on the global Alfvén speed in the corona. For example, at a height of $\approx 1.2\,R_\odot$ near active regions, the Alfvén speed is usually greater than $1000\,\mathrm{km\,s^{-1}}$ (Parker 1988; Aschwanden 2005; Morosan et al. 2016; Régnier 2015), and a CME or any other disturbance is too slow to drive a shock at these heights. Below $1.2\,R_\odot$, only five type II bursts were found, confirming that CMEs may generally be too slow to become super-Alfvénic. Even the fastest reported CMEs require some time to expand in order to reach a speed of $1000\,\mathrm{km\,s^{-1}}$ in the low corona (e.g., Mann et al. 2003; Kumari et al. 2017a; Morosan et al. 2019; Pohjolainen & Talebpour Sheshvan 2021). As the CMEs accelerate and expand, they can then reach regions

of low Alfvén speed (e.g., Warmuth et al. 2004; Morosan et al. 2022) outside the active region associated with the CME eruption. Since type II bursts are thought to be the signature of CME-driven shocks, it is likely that CME shocks also form at similar heights. The typical type II burst speed was found to be $\approx 750\,\mathrm{km\,s^{-1}}$, and type II bursts appear to have a higher speed when they have a white-light CME association (see Fig. 7a). Table 4 shows the typical parameters such as speed, duration, and drift rates for the type II bursts and the speed and width for CMEs in solar cycles 23 and 24. The large standard deviation here means that the estimated speeds, drift rates, duration, and so on are widely spread out. Because we have CMEs and type II bursts for all the phases of the solar cycles, it is expected that the deviation in mean parameters will be large. However, it is worth noting that the median value is relatively close to the mean value (Michalek et al. 2019).

When the CME propagates through the solar corona through the supercritical shock region, the shock wave creates density irregularities in the plasma. This can excite Langmuir waves (Schmidt & Cairns 2012; Mann et al. 2022). Our analysis shows that $\approx 1.7-2.3 \pm 0.3\,R_\odot$ (between 200 and 25 MHz) represents this supercritical shock region capable of generating electron beams that could excite Langmuir waves. The shock formation heights that generate type II solar radio bursts can vary depending on the properties of the CME and the surrounding coronal plasma. To verify this independently, we used the Alfvén speed, shock height, and density relation for type II bursts (for split-band type II radio bursts; Smerd et al. 1975; Vršnak et al. 2004). The type II height is directly proportional to the start frequency of the burst and the magnetic field and is inversely proportional to the Alfvén speed. For an ambient magnetic field in the range $1.5-2.0\,\mathrm{G}$ (typical B values estimated for type II bursts starting around 200 MHz; see, e.g., Dulk & McLean 1978; Kumari et al. 2017b, and the references therein), and an Alfvén-Mach number in the range $1.59 < M_A < 2.53$ (Mann et al. 2022), we obtain a shock formation height of $\approx 1.7\,R_\odot$. The lateral expansion during the early acceleration phase of a fast and wide CME (Morosan et al. 2021; Majumdar et al. 2021) can lead to the formation of supercritical shock in the height range $\approx 1.7 \pm 0.3\,R_\odot$, which can lead to the excitation of the Langmuir waves that are needed for type II solar radio burst emission. For type II bursts, the enhanced Langmuir wave level above the thermal one can be achieved rapidly (Kouloumvakos et al. 2021; Mann et al. 2022), compared to type III solar radio bursts, which require some travel time for the electrons to reach the region in which the Langmuir waves are excited (Reid 2020). This instability distance depends upon the spectral index, the electron beam velocity, the size of the acceleration site, and the temporal injection profile. For type II bursts, this occurs close to the electron acceleration sites (Schmidt & Cairns 2012; Morosan et al. 2022). We note that a few high frequency type II bursts (heights $\leq 1.5\,R_\odot$) were observed in the past two solar cycles, but the occurrence of these type II bursts were $<1\%$ of the total type II bursts. We note that individual case studies of high-frequency type II bursts are required to shed light on this (Mondal et al. 2020; Kouloumvakos et al. 2021).

This study extensively used the reports from the SWPC, which lists the manual detection of solar radio bursts from the Radio Solar Telescope Network (RSTN) for 24-h solar observations. However, we acknowledge that the RSTN spectrographs have frequency limits and lower sensitivities than the new-generation nonsolar dedicated radio telescopes, such as the LOw Frequency ARray (LOFAR; van Haarlem et al. 2013) and the Murchison Widefield Array (MWA; Tingay et al. 2013).

Table 4. Typical parameter values for type II bursts and CMEs in solar cycles 23 and 24.

Parameter	All type II			Type II with CMEs			Type II without CMEs		
	Cycle 23	Cycle 24	Total	Cycle 23	Cycle 24	Total	Cycle 23	Cycle 24	Total
Type II duration (min)									
Mean	10.4	10.7	10.5	10.7	10.8	10.7	7.5	8.4	8.2
Median	9.0	9.0	9.0	9.0	9.0	9.0	6.0	6.0	6.0
Std. dev.	6.8	9.7	7.9	8.1	6.6	10.1	6.4	6.9	4.4
Type II drift rate ($MHz\,s^{-1}$)									
Mean	0.08	0.09	0.08	0.10	0.11	0.11	0.08	0.08	0.08
Median	0.05	0.06	0.06	0.05	0.06	0.06	0.05	0.06	0.06
Std. dev	0.03	0.02	0.03	0.03	0.02	0.03	0.03	0.02	0.03
Type II speed ($km\,s^{-1}$)									
Mean	700	840	751	645	848	729	632	621	626
Median	538	671	592	490	671	563	475	456	461
Std. dev	568	716	630	773	945	815	773	848	811
Type II height ($R_\odot$)									
Mean	1.77	1.76	1.77	1.78	1.77	1.78	1.77	1.83	1.74
Median	1.71	1.62	1.69	1.73	1.64	1.69	1.69	1.85	1.67
Std. dev.	0.27	0.29	0.28	0.26	0.29	0.28	0.27	0.27	0.28
CME width (deg)									
Mean	–	–	–	160	173	165	–	–	–
Median	–	–	–	110	125	115	–	–	–
Std. dev.	–	–	–	126	122	123	–	–	–
CME speed ($km\,s^{-1}$)									
Mean	–	–	–	768	670	728	–	–	–
Median	–	–	–	584	499	546	–	–	–
Std. dev.	–	–	–	489	546	526	–	–	–

As our study makes use of two solar cycle radio bursts and CME data, we relied on the SWPC, CDAW, and SEEDS catalogs for directly extracting the onset time, duration, linear speed, angular width, start and end frequencies, and so on for the events. Because these catalogs are combinations of a manual (SWPC and CDAW) and automatic detection (SEEDS) of events, we understand that events may be misclassifed. We note that we have used the linear speed for CMEs and a constant drift rate for type II bursts, which may also lead to an error in the classification of CMEs and type II speeds. Currently, there are only two low-frequency solar-dedicated imaging instruments: the upgraded Nançay Radioheliograph (NRH; Kerdraon & Delouis 1997), and the Gauribidanur RAdioheliograPH (GRAPH; Ramesh et al. 1998), which covers the solar observations between 40 and 450 MHz from 2.5 to 16 UT at spot frequencies. This still leaves a large temporal window in which currently no solar radio imaging observations are available. With the absence of solar-dedicated imaging radio instruments, especially at low radio frequencies, one way to estimate the shock generation locations in the middle corona is by using existing density models, such as that of Newkirk (1961) (see Sect. 3.5 for details). This method has been used in several previous type II radio bursts studies in the absence of imaging observations (Vršnak et al. 2004; Vasanth et al. 2014; Ramesh et al. 2022). This study also highlights the importance of having low radio frequency solar-dedicated imaging instruments for identifying the shock-generation locations in the solar corona.

This study should be extended in the future to include imaging observations of type II radio bursts. With dedicated solar radio imaging instruments such as the upgraded NRH, the GRAPH, the expanded Owens Valley Solar Array (EOVSA; Gary et al. 2018), the Mingantu Spectral Radio Heliograph

(MUSER; Yan et al. 2021), the upcoming Daocheng Solar Radio Telescope (DSRT; Yan et al. 2022), and other powerful nonsolar radio imaging instruments such as the LOFAR, the MWA, the Long Wavelength Array (LWA; Ellingson et al. 2009), and the upgraded Giant Metrewave Radio Telescope (GMRT; Swarup 1991; Gupta et al. 2017), multiple datasets can be combined to determine the origin and source regions of these radio bursts with better accuracy. With continuous spectroscopic imaging, the source locations of these bursts relative to the CME and their speed relative to the CME flanks can also be investigated in detail to further investigate the formation heights and typical speeds of type II bursts that were also identified in this study using simple empirical models.

References

Aschwanden, M. J. 2005, Physics of the Solar Corona. An Introduction with Problems and Solutions, 2nd edn. (Chichester: Praxis Publishing Ltd)
Baumbach, S. 1937, Astron. Nach., 263, 121
Brueckner, G. E., Howard, R. A., Koomen, M. J., et al. 1995, Sol. Phys., 162, 357
Cairns, I. H., & Robinson, R. D. 1987, Sol. Phys., 111, 365
Carley, E. P., Reid, H., Vilmer, N., & Gallagher, P. T. 2015, A&A, 581, A100

Choudhary, D. P., & Moore, R. L. 2003, Geophys. Rev. Lett., 30, 2107
Chrysaphi, N., Kontar, E. P., Holman, G. D., & Temmer, M. 2018, ApJ, 868, 79
Claßen, H. T., & Aurass, H. 2002, A&A, 384, 1098
Cunha-Silva, R. D., Fernandes, F. C. R., & Selhorst, C. L. 2015, A&A, 578, A38
Dulk, G. A. 1970, PASA, 1, 308
Dulk, G. A., & McLean, D. J. 1978, Sol. Phys., 57, 279
Ellingson, S. W., Clarke, T. E., Cohen, A., et al. 2009, IEEE Proc., 97, 1421
Feynman, J., & Hundhausen, A. J. 1994, J. Geophys. Res., 99, 8451
Gary, D. E., Chen, B., Dennis, B. R., et al. 2018, ApJ, 863, 83
Gopalswamy, N. 2006, Washington DC Am. Geophys. Union Geophys. Monograph Ser., 165, 207
Gopalswamy, N., Aguilar-Rodriguez, E., Yashiro, S., et al. 2005, J. Geophys. Res. (Space Phys.), 110, A12S07
Gopalswamy, N., Thompson, W. T., Davila, J. M., et al. 2009a, Sol. Phys., 259, 227
Gopalswamy, N., Yashiro, S., Michalek, G., et al. 2009b, Earth Moon Planets, 104, 295
Gupta, Y., Ajithkumar, B., Kale, H. S., et al. 2017, Curr. Sci., 113, 707
Holman, G. D., & Pesses, M. E. 1983, ApJ, 267, 837
Howard, R. A., Moses, J. D., Vourlidas, A., et al. 2008, Space Sci. Rev., 136, 67
Kahler, S. W., Ling, A. G., & Gopalswamy, N. 2019, Sol. Phys., 294, 134
Kerdraon, A., & Delouis, J.-M. 1997, in The Nançay Radioheliograph, ed. G. Trottet, 483, 192
Klassen, A., Bothmer, V., Mann, G., et al. 2002, A&A, 385, 1078
Kouloumvakos, A., Rouillard, A., Warmuth, A., et al. 2021, ApJ, 913, 99
Kumar, P., Innes, D. E., & Cho, K.-S. 2016, ApJ, 828, 28
Kumari, A. 2022, Sol. Phys., 297, 98
Kumari, A., Ramesh, R., Kathiravan, C., & Gopalswamy, N. 2017a, ApJ, 843, 10
Kumari, A., Ramesh, R., Kathiravan, C., & Wang, T. J. 2017b, Sol. Phys., 292, 177
Kumari, A., Ramesh, R., Kathiravan, C., & Wang, T. J. 2017c, Sol. Phys., 292, 161
Kumari, A., Ramesh, R., Kathiravan, C., Wang, T. J., & Gopalswamy, N. 2019, ApJ, 881, 24
Kumari, A., Morosan, D. E., & Kilpua, E. K. J. 2021, ApJ, 906, 79
Lin, J., Mancuso, S., & Vourlidas, A. 2006, ApJ, 649, 1110
Ma, S., & Chen, H. 2020, Front. Astron. Space Sci., 7, 17
Magdalenić, J., Marqué, C., Zhukov, A. N., Vršnak, B., & Veronig, A. 2012, ApJ, 746, 152
Magdalenić, J., Marqué, C., Fallows, R. A., et al. 2020, ApJ, 897, L15
Majumdar, S., Tadepalli, S. P., Maity, S. S., et al. 2021, Sol. Phys., 296, 62
Mann, G., Classen, T., & Aurass, H. 1995, A&A, 295, 775
Mann, G., Klassen, A., Aurass, H., & Classen, H. T. 2003, A&A, 400, 329
Mann, G., Vocks, C., Warmuth, A., et al. 2022, A&A, 660, A71
Michalek, G., Gopalswamy, N., & Yashiro, S. 2019, ApJ, 880, 51
Mondal, S., Oberoi, D., & Vourlidas, A. 2020, ApJ, 893, 28
Morosan, D. E., Zucca, P., Bloomfield, D. S., & Gallagher, P. T. 2016, A&A, 589, L8
Morosan, D. E., Carley, E. P., Hayes, L. A., et al. 2019, Nat. Astron., 3, 452
Morosan, D. E., Kumari, A., Kilpua, E. K. J., & Hamini, A. 2021, A&A, 647, L12
Morosan, D. E., Pomoell, J., Kumari, A., Vainio, R., & Kilpua, E. K. J. 2022, A&A, 668, A15
Morosan, D. E., Pomoell, J., Kumari, A., et al. 2023, A&A, in press https://doi.org/10.1051/0004-6361/202245515
Nelson, G. J., & Melrose, D. B. 1985, in Solar Radiophysics: Studies of Emission from the Sun at Metre Wavelengths, eds. D. J. McLean, & N. R. Labrum (Cambridge: Cambridge University Press), 333
Newkirk, G., Jr 1961, ApJ, 133, 983
Olmedo, O., Zhang, J., Wechsler, H., Poland, A., & Borne, K. 2008, Sol. Phys., 248, 485
Parker, E. N. 1988, ApJ, 330, 474
Patel, B. D., Joshi, B., Cho, K.-S., & Kim, R.-S. 2021, Sol. Phys., 296, 142
Pohjolainen, S., & Talebpour Sheshvan, N. 2021, Sol. Phys., 296, 81
Ramesh, R., Subramanian, K. R., Sundararajan, M. S., & Sastry, C. V. 1998, Sol. Phys., 181, 439
Ramesh, R., Kathiravan, C., Kartha, S. S., & Gopalswamy, N. 2010, ApJ, 712, 188
Ramesh, R., Kathiravan, C., & Chellasamy, E. E. 2022, ApJ, 932, 48
Ramesh, R., Kathiravan, C., & Kumari, A. 2023, ApJ, 943, 43
Régnier, S. 2015, A&A, 581, A9
Reid, H. A. S. 2020, Front. Astron. Space Sci., 7, 56
Roberts, J. A. 1959, Aust. J. Phys., 12, 327
Saito, K., Poland, A. I., & Munro, R. H. 1977, Sol. Phys., 55, 121
Salas-Matamoros, C., & Klein, K.-L. 2020, A&A, 639, A102
Schmidt, J. M., & Cairns, I. H. 2012, J. Geophys. Res. (Space Physics), 117, A04106
SILSO World Data Center 1996–2019, International Sunspot Number Monthly Bulletin and Online Catalogue
Smerd, S. F. 1970, PASA, 1, 305
Smerd, S. F., Sheridan, K. V., & Stewart, R. T. 1975, App. Lett., 16, 23
Swarup, G. 1991, in IAU Colloq. 131: Radio Interferometry. Theory, Techniques, and Applications, eds. T. J. Cornwell, & R. A. Perley, ASP Conf. Ser., 19, 376
Tingay, S. J., Goeke, R., Bowman, J. D., et al. 2013, PASA, 30, e007
van Haarlem, M. P., Wise, M. W., Gunst, A. W., et al. 2013, A&A, 556, A2
Vasanth, V., Umapathy, S., Vršnak, B., Žic, T., & Prakash, O. 2014, Sol. Phys., 289, 251
Vourlidas, A., Balmaceda, L. A., Stenborg, G., & Dal Lago, A. 2017, ApJ, 838, 141
Vršnak, B., Magdalenić, J., & Zlobec, P. 2004, A&A, 413, 753
Warmuth, A., Vršnak, B., Magdalenić, J., Hanslmeier, A., & Otruba, W. 2004, A&A, 418, 1101
Yan, J., Wu, L., Yang, Y., & Wu, J. 2022, in 44th COSPAR Scientific Assembly. Held 16–24 July, 44, 1886
Yan, Y., Chen, Z., Wang, W., et al. 2021, Front. Astron. Space Sci., 8, 20
Yashiro, S., Gopalswamy, N., Michalek, G., et al. 2004, J. Geophys. Res. (Space Physics), 109, A07105
Yashiro, S., Michalek, G., & Gopalswamy, N. 2008, Ann. Geophys., 26, 3103
Zhang, J., Dere, K. P., Howard, R. A., & Bothmer, V. 2003, ApJ, 582, 520
Zlobec, P., Messerotti, M., Karlicky, M., & Urbarz, H. 1993, Sol. Phys., 144, 373
Zucca, P., Morosan, D. E., Rouillard, A. P., et al. 2018, A&A, 615, A89